

Modern Physics Letters A  
© World Scientific Publishing Company

## Results on neutrinoless double beta decay from GERDA Phase I

CARLA MACOLINO

*INFN, Laboratori Nazionali del Gran Sasso, S.S. 17 BIS km. 18.910  
67010 Assergi L'Aquila, Italy \**

Received (Day Month Year)

Revised (Day Month Year)

The GERmanium Detector Array, GERDA, is designed to search for neutrinoless double beta ( $0\nu\beta\beta$ ) decay of  $^{76}\text{Ge}$  and it is installed in the Laboratori Nazionali del Gran Sasso (LNGS) of INFN, Italy. In this review, the detection principle and detector setup of GERDA are described. Also, the main physics results by GERDA Phase I, are discussed. They include the measurement of the half-life of  $2\nu\beta\beta$  decay, the background decomposition of the energy spectrum and the techniques for the discrimination of the background, based on the pulse shape of the signal. In the last part of this paper, the estimation of a limit on the half-life of  $0\nu\beta\beta$  ( $T_{1/2}^{0\nu} > 2.1 \cdot 10^{25}$  yr at 90% C.L.) and the comparison with previous results are discussed. GERDA data from Phase I strongly disfavour the recent claim of  $0\nu\beta\beta$  discovery, based on data from the Heidelberg-Moscow experiment.

*Keywords:* Neutrino mass and mixing; Neutrinoless double beta decay; Majorana neutrino; enriched Ge detectors; GERDA experiment

PACS 14.60.Pq; 23.40.-s; 21.10.Tg

### 1. Introduction and Science Motivation

The nature and properties of the neutrino have an important impact on our knowledge of the Universe. Recent results about neutrino flavour oscillations have shown evidence of non-zero neutrino mass and have provided values of the squared masses of the neutrino mass eigenstates,  $\Delta m^2$ . Neutrinoless double beta decay ( $0\nu\beta\beta$ ) can give additional information on the possible “Majorana” nature of the neutrino, i.e. when each neutrino eigenstate  $\nu_i$  coincides with its anti-particle  $\bar{\nu}_i$ . In such a case, lepton number would be no longer conserved and physics beyond the Standard Model would be required. Additionally, neutrinoless double beta decay can give an indirect measurement on the absolute mass of neutrinos and shed light to the hierarchy of neutrino masses. This is very important when compared to similar bounds from Cosmic Microwave Background (CMB) and Large Scale Structures (LSS) in the Universe.

\*E-mail address: carla.macolino@lngs.infn.it

Two-neutrino double beta decay ( $2\nu\beta\beta$ ) is a second-order process in the Standard Model in which a nucleus changes its atomic number  $Z$  by two units, with the emission of two beta particles and two neutrinos, e.g.:

$$(A, Z) \rightarrow (A, Z + 2) + 2e^- + 2\bar{\nu}_e. \quad (1)$$

Such a decay can be observed for some even-even nuclei when ordinary beta decay is energetically prohibited. This decay is very rare with typical half-lives ranging from  $\sim 10^{19}$  to  $\sim 10^{21}$  yr. Neutrinoless double beta decay can be viewed as the ordinary two-neutrino double beta decay where no neutrino is emitted in the final state:

$$(A, Z) \rightarrow (A, Z + 2) + 2e^-. \quad (2)$$

While the  $2\nu\beta\beta$  process is not forbidden by any conservation law in the Standard Model,  $0\nu\beta\beta$  can only occur if the neutrino has a non-zero mass and is a Majorana particle. Theoretical models predict that  $0\nu\beta\beta$  could be mediated by a light Majorana neutrino. Indeed, within the  $SU_L(2) \times U(1)$  Standard Model of electroweak interactions,  $0\nu\beta\beta$  can be seen as the exchange of a virtual neutrino between two neutrons in the nucleus; the Majorana particle emitted by the first neutron contains two helicity components: a dominant negative one and a very small positive one. The latter is seen as an antineutrino when absorbed by the second neutron. This is only possible if the neutrino is not in a pure helicity state (therefore it has mass) and it is identical to its anti-particle. For these reasons, the observation of neutrinoless double beta decay would definitely demonstrate the Majorana nature of the neutrino. In addition, the effective mass of the Majorana neutrino can be measured and the hierarchy of the mass eigenstates can be investigated.

The effective Majorana neutrino mass is related to the half-life of the decay by the following relation:

$$\frac{1}{T_{1/2}^{0\nu}(A, Z)} = F^{0\nu} \cdot |\mathcal{M}^{0\nu}|^2 \cdot \left| \frac{m_{\beta\beta}}{m_e} \right|^2, \quad (3)$$

where  $m_e$  is the electron mass,  $F^{0\nu}$  is the phase space factor,  $\mathcal{M}^{0\nu}$  is the nuclear matrix element (NME) and  $m_{\beta\beta}$  is the effective Majorana electron neutrino mass:

$$m_{\beta\beta} \equiv |U_{e1}|^2 m_1 + |U_{e2}|^2 m_2 e^{i\phi_2} + |U_{e3}|^2 m_3 e^{i\phi_3}, \quad (4)$$

where  $m_i$  are the masses of the neutrino mass eigenstates,  $U_{ei}$  the elements of the neutrino mixing matrix and  $e^{i\phi_2}$  and  $e^{i\phi_3}$  the relative Majorana CP phase factors. The  $0\nu\beta\beta$  decay can be experimentally observed as a narrow peak in the end-point of the  $2\nu\beta\beta$  decay energy spectrum, corresponding to the Q-value ( $Q_{\beta\beta}$ ) of the decay. The number of counts in the peak would allow to quantify the decay rate of the process or, in case of no signal, to set a lower limit on it, via the relation:

$$T_{1/2}^{0\nu} = \frac{\ln 2 \cdot N_A}{N^{0\nu}} \cdot \varepsilon \cdot \epsilon \cdot \frac{k}{M_A} \quad (5)$$

with  $N_A$  the Avogadro's number,  $\varepsilon$  the total exposure (detector mass  $\times$  live time),  $\epsilon$  the detection efficiency,  $k$  the enrichment fraction of the enriched material ( $k$  corresponds to the fraction of  $^{76}\text{Ge}$  atoms ( $f_{76}$ ) in GERDA) and  $M_A$  its atomic mass

(75.6 g for  $^{76}\text{Ge}$ ).  $N^{0\nu}$  is the observed signal strength or the corresponding upper limit.

The GERDA experiment<sup>6,7</sup> searches for neutrinoless double beta decay of  $^{76}\text{Ge}$ , in which  $^{76}\text{Ge}$  ( $Z=32$ ) would decay into  $^{76}\text{Se}$  ( $Z=34$ ) and two electrons. The detectors implemented in the GERDA setup are semiconductors made from material with an isotope fraction of  $^{76}\text{Ge}$  enriched to about 86% ( $^{enr}\text{Ge}$ ), which acts as both the  $\beta\beta$  decay source and a  $4\pi$  detector. The detectors are characterized by a very good energy resolution, which allows a clear distinction of the neutrinoless double beta peak at  $Q_{\beta\beta}=2039$  keV, which is an energy region that is nearly background-free. Prior to the latest GERDA results, the best limits for  $0\nu\beta\beta$  decay in  $^{76}\text{Ge}$  were provided by the Heidelberg-Moscow (HdM)<sup>8</sup> and IGEX<sup>9</sup> enriched  $^{76}\text{Ge}$  experiments, that yielded lower half-life limits of  $T_{1/2} > 1.9 \cdot 10^{25}$  yr and  $T_{1/2} > 1.6 \cdot 10^{25}$  yr respectively, corresponding to an upper limit on the effective Majorana mass of  $|m_{\beta\beta}| < 0.33 \div 1.35$  eV; the range in mass arises from the estimated uncertainty in the nuclear matrix elements. A subgroup of the HdM collaboration claimed the observation of  $0\nu\beta\beta$  with a half-life of  $T_{1/2}^{0\nu} = 1.19_{-0.23}^{+0.37} \cdot 10^{25}$  yr, corresponding to a range for  $|m_{\beta\beta}|$  between 0.24 and 0.58 eV, with a central value of 0.44 eV<sup>10</sup>. In a more sophisticated analysis, the authors found a value for the half-life  $T_{1/2}^{0\nu} = 2.23_{-0.31}^{+0.44} \cdot 10^{25}$  yr<sup>11</sup>, though some inconsistencies associated to this result have been pointed out in Ref. 12.

The aim of the Phase I of the GERDA experiment was to verify the previous results and to reach a much higher sensitivity than previous experiments. The plan for GERDA Phase II is to reach the target sensitivity of  $T_{1/2}^{0\nu} = 1.4 \cdot 10^{26}$  yr, with an increased total mass of the enriched material and a reduced background level.

The outline of the paper is the following: in Sect. 2 it is described the experimental setup of GERDA at LNGS; the main results concerning  $2\nu\beta\beta$  and  $0\nu\beta\beta$  decays are discussed in Sects. 3 and 6. The background characterization is described in Sec. 4 and, finally, pulse-shape discrimination, used to disentangle the signal from background events, is discussed in Sec. 5.

## 2. The GERDA experimental setup

The detection concept of GERDA is implemented by operating bare  $^{enr}\text{Ge}$  (Ge detectors enriched in  $^{76}\text{Ge}$ ) inside a cryostat containing cryogenic liquid argon (LAr), surrounded by an additional shield of ultra-pure water. Liquid argon, indeed, acts both as the coolant medium for the  $^{enr}\text{Ge}$  detectors and the shield against external gamma radiation<sup>1</sup>. The Ge detectors are suspended in the cryostat by an array of strings. In Fig. 1 an artist's view of the GERDA detector is shown. The cryostat is a steel vessel of 4 m diameter with a copper lining, to reduce gamma radiation from the steel vessel. However, radon can emanate from the vessel walls and be convected close the Ge diodes. This can be prevented by separating the central volume from the rest of the cryostat by a 3 m high and 750 mm large cylinder, made of a 30  $\mu\text{m}$  copper foil ("radon shroud"). A large tank (8.5 m high and 10 m of diameter) filled with ultra-pure water surrounds the cryostat and provides a 3 m thick



Fig. 1. An artist's view of the GERDA detector. The array of Ge detectors is not to scale. From Ref. 1, with kind permission of The European Physical Journal (EPJ).

water buffer around the cryostat. The water buffer is a multi-purpose medium; it is used to: (i) moderate and absorb neutrons, (ii) attenuate the flux of external  $\gamma$  radiation, (iii) provide the Cherenkov medium for the detection of muons and (iv) provide a backup system for the disposal of the argon gas in case of emergency. To easily insert the detector strings and the calibration sources into the cryostat, without increasing the contamination of the cryogenic volume, a cleanroom and a lock are located on top of the vessel. The water tank is instrumented with 66 PMTs, to detect Cherenkov light produced by muon induced showers in the water buffer. Cherenkov and scintillation signals, the latter provided by an array of 36 plastic scintillator panels placed on the roof of the cleanroom, are combined as a muon veto for the data acquisition according to a logic OR.

Data acquisition of GERDA Phase I started on November, 2011 with 8 p-type  $^{enr}\text{Ge}$  semi-coaxial (HPGe) detectors, 4 coming from the previous HdM experiment, 1 not enriched from the GENIUS-Test-Facility<sup>13</sup> at Gran Sasso and 3 from the IGEX experiment, with a total mass of about 20.7 kg (17.7 kg enriched and 3 kg not enriched). On July 2012, 5 Broad Energy GERmanium<sup>a</sup> (BEGes) diodes, with total mass of about 3.6 kg and foreseen for the Phase II of the experiment, were also put in place, in order to test them in a realistic environment. The detector array has a structure made of individual strings, each of them containing up to five independent Ge detectors. The energy scale is determined by calibrating with  $^{228}\text{Th}$  sources on a weekly basis and was stable during the entire data acquisition period. Indeed, the differences between the reconstructed peaks of the  $^{228}\text{Th}$  spectrum and the ones from the calibration curves are smaller than 0.3 keV. In the very first

<sup>a</sup>The Broad Energy GERmanium Detectors were manufactured in Olen, Belgium by Canberra.

phase of GERDA data taking, a very high background was observed ( $18 \cdot 10^{-2}$  counts/(keV·kg·yr)). Also, the line at 1525 keV from  $^{42}\text{K}$ , the progeny of  $^{42}\text{Ar}$ , had an intensity in the energy spectrum much higher than expected<sup>14</sup>. These observations suggested the hypothesis that charged ions of  $^{42}\text{K}$  drifted in the electric field produced by the 3 to 4 kV bias of the bare Ge diodes. For this reason the strings of detectors were enclosed into 60  $\mu\text{m}$  thick copper cylinders (“mini-shrouds”).

### 3. Measurement of the half-life of $2\nu\beta\beta$ decay of $^{76}\text{Ge}$ with GERDA

The measurement of the half-life  $T_{\beta\beta}^{2\nu}$  of two-neutrino double beta decay ( $2\nu\beta\beta$ ) of  $^{76}\text{Ge}$  is of extreme interest for different reasons. Firstly, the accurate measurement of  $2\nu\beta\beta$  half-life allows to test the predictions on  $\mathcal{M}^{2\nu}$  based on charge exchange experiments<sup>21,22</sup> and, therefore, to better understand the nuclear aspects of the decay. Secondly, as suggested in Refs. 15, 16, 17, 18, 19, 20, the nuclear matrix elements  $\mathcal{M}^{0\nu}$  and  $\mathcal{M}^{2\nu}$ , for  $0\nu\beta\beta$  and  $2\nu\beta\beta$  decays respectively, are related; therefore, the estimation of  $T_{\beta\beta}^{2\nu}$  can also constrain the value of  $\mathcal{M}^{0\nu}$ , that is subject to theoretical uncertainties. The considered GERDA data set consists of 8796 events, taken between November 2011 and March 2012, from the six enriched semi-coaxial detectors, with a total collected exposure of 5.04 kg·yr. The very low energy part of the spectrum is dominated by the  $\beta^-$  decay of  $^{39}\text{Ar}$ , produced by cosmogenic activation of natural argon in the atmosphere, with a Q-value of 565 keV. At higher energies the spectrum is completely dominated by the  $2\nu\beta\beta$  decay. For this reason, the search for  $2\nu\beta\beta$  decay the analysis was performed for events with energy in the range between 600 and 1800 keV. According to Monte Carlo simulations, the probability for the  $2\nu\beta\beta$  process to release energy above 1800 keV in the GERDA detectors is 0.02%. The analysis of the energy spectra from the six semi-coaxial diodes was based on a maximum likelihood approach<sup>24</sup>, fitting each energy spectrum with a global model which considers the  $2\nu\beta\beta$  decay of  $^{76}\text{Ge}$  and three independent background contributions:  $^{42}\text{K}$ ,  $^{214}\text{Bi}$  and  $^{40}\text{K}$ .  $^{42}\text{K}$  is a progeny of  $^{42}\text{Ar}$ , while  $^{214}\text{Bi}$  (originated from the  $^{238}\text{U}$  decay series) and  $^{40}\text{K}$  are gamma emitters from the environmental radioactivity; their gamma lines are observed in the experimental spectrum at 1525 keV, 1764 keV and 1460 keV, respectively. Other background contributions are not included in the fit, since their gamma lines are not clearly distinguished in the spectrum, either because of low statistical significance or because they are not observed in all the spectra. The energy spectra for the model components (signal plus backgrounds) were obtained from Monte Carlo simulations, for each detector, by using the MAGE framework<sup>25</sup> based on GEANT4<sup>26,27</sup>. The energy distribution of the two electrons was simulated according to the model<sup>28</sup> implemented in the DECAY0 code<sup>29</sup>. While the activity of  $^{42}\text{K}$  was assumed to be uniformly distributed in the LAr volume,  $^{40}\text{K}$  and  $^{214}\text{Bi}$  emitters are assumed as “close sources”, i.e. located in the detector assembly. The ratio of the intensities of the  $^{214}\text{Bi}$   $\gamma$  lines observed in the energy spectrum is consistent with this hypothesis. The fit parameters were

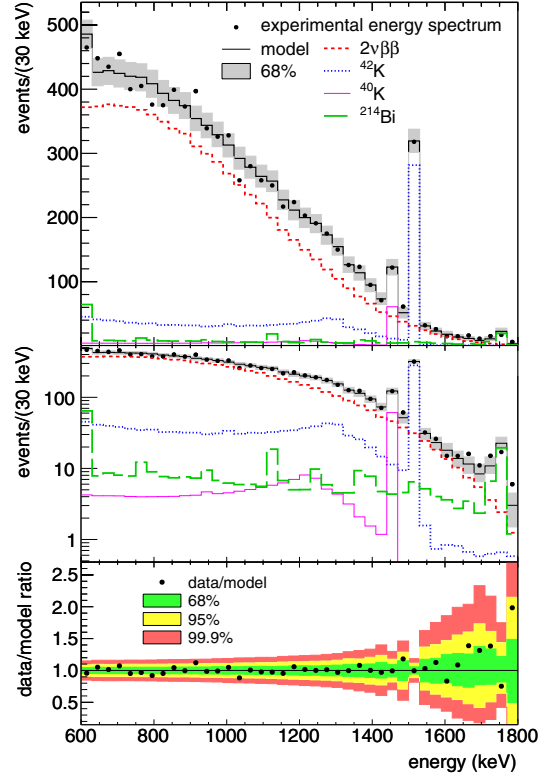


Fig. 2. Upper and middle panels: Experimental data (markers) and the best fit model (black histogram) in linear and logarithmic scale (Data refer to the sum of the six detectors). Individual contributions from the  $2\nu\beta\beta$  decay (red),  $^{42}\text{K}$  (blue),  $^{40}\text{K}$  (purple) and  $^{214}\text{Bi}$  (green) are also shown. The shaded band indicates the 68% probability range for the data calculated from the expected event counts of the best fit model. Lower panel: ratio between experimental data and the prediction of the best fit model as a function of the energy. Plot from Ref. 2. ©IOP Publishing. Reproduced by permission of IOP Publishing. All rights reserved.

taken to be the half-life of the  $2\nu\beta\beta$  decay, common to the six spectra, and the intensities of the background components (considered as independent for each detector). Additionally, the active masses and the  $^{76}\text{Ge}$  abundance of each detector were considered as nuisance parameters and integrated at the end of the analysis. The spectral fit was performed using the Bayesian Analysis Toolkit<sup>30</sup>. The prior probability density function (PDF) for  $T_{1/2}^{2\nu}$  was considered as a flat distribution between 0 and  $10^{22}$  yr, while the prior PDFs for the active mass fraction and the  $^{76}\text{Ge}$  isotopic abundance of each detector were modelled according to a Gaussian distribution.

In Fig. 2 the best fit model is shown, together with experimental data for the sum of the six detectors and the individual components obtained from the fit. The best fit model gives an expectation of 8797.0 events divided as follows: 7030.1 (79.9%)

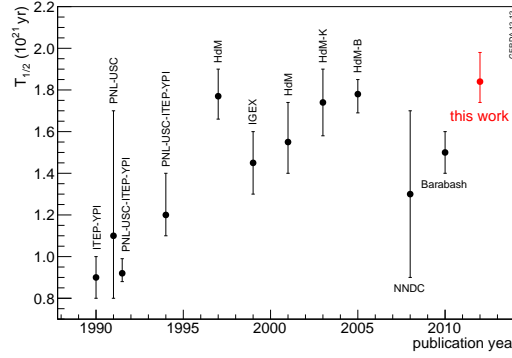


Fig. 3.  $T_{1/2}^{2\nu}$  experimental values for  $^{76}\text{Ge}$  from previous experiments compared to the GERDA result. Plot from Ref. 2. ©IOP Publishing. Reproduced by permission of IOP Publishing. All rights reserved.

from the  $2\nu\beta\beta$  decay of  $^{76}\text{Ge}$ , 1244.6 (14.1%) from  $^{42}\text{K}$ , 335.5 (3.8%) from  $^{214}\text{Bi}$  and 186.8 (2.1%) from  $^{40}\text{K}$ . The average signal to background ratio is 4:1. The model reproduces very well the experimental data, with a  $p$ -value of the fit equal to  $p=0.77$ . The best estimate of the derived half-life of  $2\nu\beta\beta$  is

$$T_{1/2}^{2\nu} = (1.84^{+0.09}_{-0.08} \text{ fit } ^{+0.11}_{-0.06} \text{ syst}) \times 10^{21} \text{ yr} = (1.84^{+0.14}_{-0.10}) \times 10^{21} \text{ yr}, \quad (6)$$

where the fit and the systematical uncertainties are summed in quadrature.

The fit's error on  $T_{1/2}^{2\nu}$  includes both the statistical and the error associated to the marginalization of the nuisance parameters. The systematic error on  $T_{1/2}^{2\nu}$  includes uncertainties related to the background model (position and distribution of the sources), uncertainties due to Monte Carlo simulation details and errors related to data acquisition and data handling. The combination in quadrature of all these contributions gives a systematic uncertainty of  $^{+6.2}_{-3.3}\%$ , which corresponds to  $^{+0.11}_{-0.06} \times 10^{21}$  yr. The comparison between the half-life estimated by GERDA and those from previous measurements for  $^{76}\text{Ge}$  is shown in Fig. 3. Almost all the estimated values for  $T_{1/2}^{2\nu}$  tend to be larger with the publication year, probably because of an increasing signal-to-background ratio, which makes the effect of background modelling and subtraction less important. with the estimate given in in Ref. 31 (labelled as “Barabash”); indeed, if  $T_{1/2}^{2\nu}$  were as short as  $1.5 \cdot 10^{21}$  yr, almost all counts detected in the range 600-1800 keV should be due to  $2\nu\beta\beta$  (expected: 8782.7, observed: 8976), with nearly no possible contribution from background. On the other hand, the GERDA estimation is in better agreement with the two most recent results (“HdM-K” and “HdM-B”) reported in Refs. 32 and 33, based on the re-analysis of HdM data.

The experimental nuclear matrix element for the  $2\nu\beta\beta$  decay of  $^{76}\text{Ge}$  was derived from the measured the half-life, using the phase space factors from the recently improved electron wave functions<sup>34</sup>:  $\mathcal{M}^{2\nu} = 0.133^{+0.004}_{-0.005} \text{ MeV}^{-1}$ . In Ref. 15 the matrix

elements  $\mathcal{M}^{2\nu}$  and  $\mathcal{M}^{0\nu}$  for  $^{76}\text{Ge}$  were related in the QRPA approximation. Notice that, the half-life measured by GERDA corresponds to a value for  $\mathcal{M}^{2\nu}$  that is 11% smaller than the one quoted in ref. 15. Using that value for  $\mathcal{M}^{2\nu}$ , and the relation between  $\mathcal{M}^{2\nu}$  and  $\mathcal{M}^{0\nu}$  showed in Ref. 16, the predicted half-life for  $0\nu\beta\beta$  is about 15% larger but still well within the uncertainty of the model calculation. The nuclear matrix element for  $2\nu\beta\beta$  decay of  $^{76}\text{Ge}$  was also estimated from charge exchange reactions<sup>21,22</sup> ( $d,^2\text{He}$ ) and ( $^3\text{He},t$ ). Their value is larger, but still consistent, than the one derived by the GERDA measurement.

#### 4. The background of GERDA Phase I

In order to extract a possible signal at  $Q_{\beta\beta}$  or, in case of no event, to determine a lower limit on the half-life of the  $0\nu\beta\beta$  process, it is important to understand the different contributions observed in the energy spectrum. The identification of these contributions is also crucial to derive a strategy for background suppression. The background decomposition of the GERDA energy spectrum was done considering data for a total exposure of 16.70 kg·yr. The data were divided according to the different Background Index (BI) in the region around  $Q_{\beta\beta}$ , defined as the number of counts per keV·kg·yr; in particular, *SILVER-coax* are data from semi-coaxial detectors collected after the deployment of BEGe detectors in LAr (1.30 kg·yr exposure), *GOLD-coax* are data from semi-coaxial detectors except *SILVER-coax* data (15.40 kg·yr exposure) and *BEGe* are data from the BEGe detectors<sup>3</sup> (1.80 kg·yr exposure).

The energy spectra from the enriched semi-coaxial detectors, from the BEGes and from the detector with natural germanium are shown in Fig. 4. In the low energy part, up to 565 keV, the energy spectra are dominated by the  $\beta$ -decay of cosmogenic  $^{39}\text{Ar}$ . Some differences in the shape of the low energy spectrum is expected between the semi-coaxial and BEGe detectors because of the slight difference of geometry and of the  $n^+$  dead layer thicknesses. In the region between 600 and 1500 keV, the enriched detector spectra are dominated by the continuous spectrum of the  $2\nu\beta\beta$  decay<sup>2</sup>.

All spectra show  $\gamma$  lines from the decay of  $^{40}\text{K}$  and  $^{42}\text{K}$ , while enriched detectors spectra show lines also from  $^{60}\text{Co}$ ,  $^{208}\text{Tl}$ ,  $^{214}\text{Bi}$ ,  $^{214}\text{Pb}$  and  $^{228}\text{Ac}$ . Just a single line from  $^{214}\text{Bi}$  appears clearly in the spectrum between 2000 and 2600 keV (at 2204 keV with 17.3 counts). Additional  $\gamma$  lines from  $^{214}\text{Bi}$  are not expected in this range due to the much lower branching ratios of the transitions (the strongest line at 2448 keV would give 5.5 counts). Different peak-like structures appear in the high energy part of the spectra; in particular, the important peak-like structure at 5.3 MeV for the enriched detectors can be attributed to the  $\alpha$  decay of  $^{210}\text{Po}$  on the  $p^+$  surface of the detectors. Additional other peak-like structures, due the  $\alpha$  decays on the  $p^+$  surfaces, appear at 4.7 MeV (for  $^{226}\text{Ra}$ ), 5.4 MeV (for  $^{222}\text{Rn}$ ) and 5.9 MeV (for  $^{218}\text{Po}$ ).

Some of the background components identified in the spectra can be traced back,



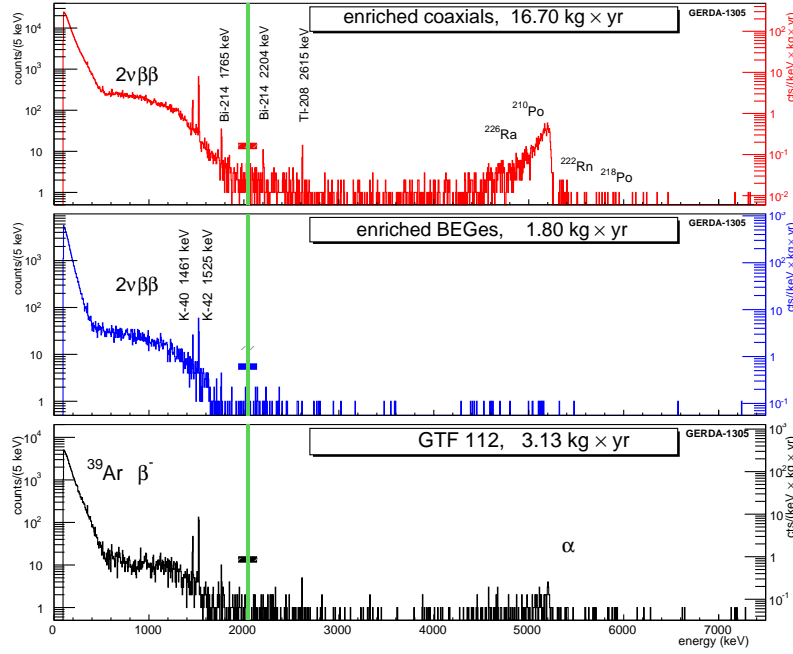


Fig. 4. Spectra from enriched semi-coaxial (top), enriched BEGe (middle) and non-enriched (bottom) detectors of GERDA Phase I. The green line indicates the  $Q_{\beta\beta} \pm 20$  keV region of blinded data. The bar on the right side of the y-axis indicates the corresponding background index. Plots from Ref. 3, with kind permission of The European Physical Journal (EPJ).

from the the material screening, nearby the detector and from the electronics. Indeed,  $^{228}\text{Ac}$  and  $^{228}\text{Th}$  are expected in the front end electronics and in the detector suspension system,  $^{224}\text{Ra}$  daughters  $^{214}\text{Bi}$  and  $^{214}\text{Pb}$  are expected close to the detectors,  $^{40}\text{K}$  is expected from the detector assembly and  $^{42}\text{K}$  from the  $\beta$ -decay of  $^{42}\text{Ar}$ . The latter is homogeneously distributed inside LAr, though  $^{42}\text{K}$  ions can drift in the electric fields surrounding the detectors. Neutron and muon fluxes are expected to be of the order of  $10^{-5}$  cts/(keV·kg·yr) and  $10^{-4}$  cts/(keV·kg·yr) respectively<sup>35,36</sup> and their contribution can be neglected. Finally, isotopes like  $^{76}\text{Ge}$  (via neutron capture),  $^{206}\text{Pb}$  (by inelastic neutron scattering) and  $^{56}\text{Co}$  (via decay) could also cause  $\gamma$  show up as peaks in the vicinity of  $Q_{\beta\beta}$ , however these components either have very short half-lives or simply are not associated to other peaks that should be observed in the GERDA spectrum.

All background components previously discussed were simulated in the the MAGE framework<sup>25</sup> based on GEANT4<sup>26,27</sup> implementing also the GERDA Phase I detectors arrangement in four strings. The contamination contributions were simulated into the different hardware components of the detector setup: inside the germanium, on the  $p^+$  and  $n^+$  surfaces of the detectors, in the liquid argon close to the  $p^+$  surface, homogeneously distributed in the LAr, in the detector assembly, in the

mini-shroud, in the radon shroud and in the heat-exchanger. The simulated energy spectra were smeared with a Gaussian distribution with Full Width Half Maximum (FWHM) equal to the detector resolution.

Two global models were obtained through a Bayesian fit of the simulated energy spectrum to the measured one: a “minimum model” fit, where only a minimum amount of background components were considered, and a “maximum model” fit containing all the possible contributions. In the “minimum model” only background sources located close to the detectors (up to 2cm), were considered. In the “maximum model” further medium and large distance background components, assumed to be present in different hardware components of the experiment, were added to the model. Once fitted the models to the data, the result was used to derive the activities of the different background contributions. It turns out that data are well described by both models and that there is no unique determination of the count rates of the different background components. However, the largest fraction of background comes from close sources even when medium and large distance sources are added, especially on the p+ and n+ surfaces. The best fit for the “minimum model” and the energy spectrum of the *GOLD-coax* data set are shown in Fig. 5 for different energies in the range between 570 keV and 3750 keV. In the energy region between 570 keV and 1500 keV, the spectrum is well described by the same background

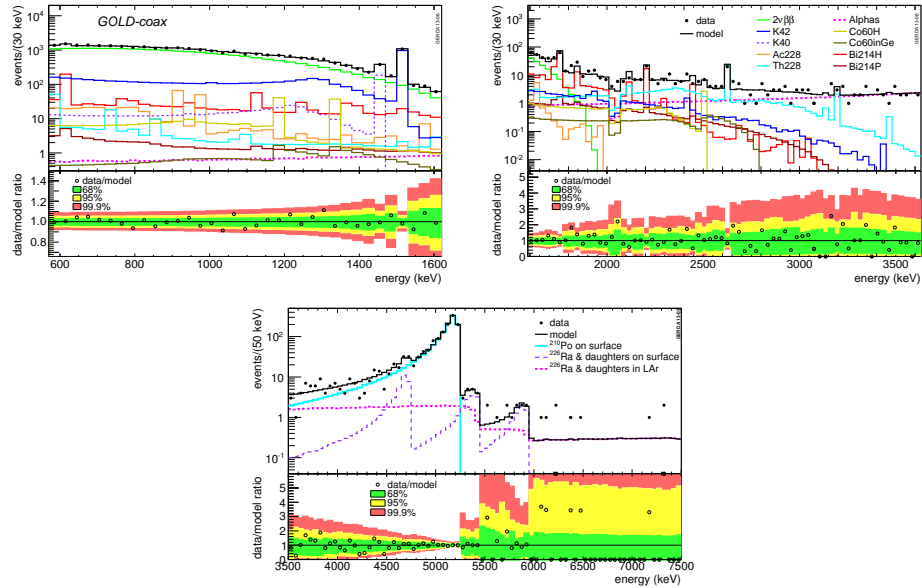


Fig. 5. Background decomposition for data from *GOLD-coax* data set, according to the best fit minimum model. The lower panel shows the ratio between experimental data and the prediction from the best fit model, together with the 68% (green), 95% (yellow) and 99.9% (red) probability bands. Plots from Ref. 3, with kind permission of The European Physical Journal (EPJ).

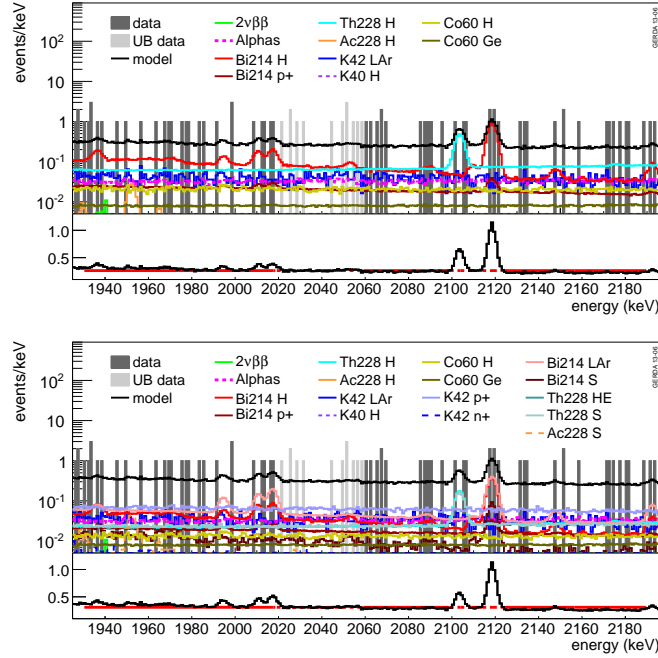


Fig. 6. Energy spectrum for experimental data together with the minimum (top) and maximum (bottom) models around  $Q_{\beta\beta}$  for the *GOLD-coax* data set. The upper panels show the individual contributions and the lower panels show the model fitted with a constant. Plots from Ref. 3, with kind permission of The European Physical Journal (EPJ).

components considered for the  $2\nu\beta\beta$  analysis, i.e.  $^{42}\text{K}$ ,  $^{40}\text{K}$  and  $^{214}\text{Bi}$ . In the range between 3.5 MeV and 7.5 MeV, the background is expected to come mainly from  $\alpha$  emitting isotopes in the  $^{226}\text{Ra}$  decay chain, which can be broken at  $^{210}\text{Pb}$  (with half-life of 22.3 yr) and at  $^{210}\text{Po}$  (with half-life of 138.4 days). The time distribution of the events confirms the presence of  $^{210}\text{Po}$ , since data are well fit very by a decreasing exponential plus a constant distribution and the Bayesian fit with a non-informative prior for the half-life gives  $T_{1/2}=130.4\pm22.4$  days, which is in very good agreement with the half-life of  $^{210}\text{Po}$ . The spectrum is described well by  $^{210}\text{Po}$  on the surface of the detectors and  $^{226}\text{Ra}$  and its daughter nuclei on the  $p^+$  surface and in liquid argon. The best fits in the region around the  $Q_{\beta\beta}$  value are shown in figure 6, for both the “minimum” and the “maximum” model. The predicted background around  $Q_{\beta\beta}$  is flat, with no contribution from  $\gamma$  peaks. The resulting BI for the “minimum model” is  $1.85^{+0.08}_{-0.09} \times 10^{-2}$  cts/(keV·kg·yr), while for the “maximum model” is  $2.19^{+0.19}_{-0.12} \times 10^{-2}$  cts/(keV·kg·yr). The Background Index for *GOLD-coax* data has been evaluated in the energy window between 1930 and 2190 keV, with the exclusion of the central 40 keV window around  $Q_{\beta\beta}$  and of the  $\pm 5$  keV regions around the position of  $\gamma$  lines, expected from the background model (single escape

peak from  $^{208}\text{Tl}$  at 2104 keV and  $\gamma$  line at 2119 keV from  $^{214}\text{Bi}$ ). The measured value ( $\text{BI}=1.75^{+0.26}_{-0.24}\times 10^{-2}$  cts/(keV·kg·yr)) is in good agreement with the values predicted by the two models. In both cases, the most significant contributions to the background in the  $Q_{\beta\beta}$  region, come from  $^{214}\text{Bi}$  and  $^{228}\text{Th}$  in the detector assembly, from  $^{42}\text{K}$ , homogeneously distributed in LAr, and from  $\alpha$  emitters.

Concerning the background model for *BEGe* data, only a qualitative analysis was possible, since the exposure collected with these detectors was small. Considering the “minimum model” fit, with the addition of  $^{68}\text{Ge}$  decays in germanium and  $^{42}\text{K}$  decays on the  $n^+$  surface, the dominant background source around  $Q_{\beta\beta}$  is given by  $^{42}\text{K}$  on the  $n^+$  surface. This contribution is expected to be more important in *BEGe* detectors than the semi-coaxial ones because of a thinner dead layer.

In order to keep analysis cuts and procedures not biased, GERDA Phase I data were blinded (not processed) in a 40 keV energy window between 2019 keV and 2049 keV, up to the collection of 20 kg·yr exposure. Eventually, data were partially unblinded with a still-blinded window of 10 keV for the *GOLD-coax* and *SILVER-coax* subsets, and 8 keV window for the *BEGe* data set. The models show good agreement with the observed spectrum around  $Q_{\beta\beta}$ . In the unblinded 30 keV window for *GOLD-coax* data, 8.6 events were predicted by the “minimum model” fit and 10.3 by the “maximum” one, while 13 events were observed.

## 5. Pulse shape discrimination of GERDA Phase I data

In the GERDA detectors,  $0\nu\beta\beta$  events have a peculiar pulse shape which can be discriminated from background events. Indeed, the two electrons from  $0\nu\beta\beta$  decay deposit their energy by ionization at one location in the detectors and those events are called Single Site Events (SSE). Conversely, the background is mostly due to  $\gamma$  induced events and their energy is deposited at multiple locations in the detectors, via multiple Compton scatterings; the  $\gamma$  can, indeed, travel several centimeters. Therefore, such events are called Multi Site Events (MSE). The discrimination of  $0\nu\beta\beta$  events, based on the shape of the recorded pulses, is called Pulse Shape Discrimination (PSD). In GERDA Phase I two different methods for PSD are used, according to the different characteristics of the pulses and electric field distributions of semi-coaxial and *BEGe* detectors<sup>4</sup>. Concerning *BEGes*, the ratio between the maximum  $A$  of the current pulse (obtained by numerical differentiation of the charge pulse) and the energy  $E$  of the event (corresponding to the maximum of the charge pulse) is the discrimination parameter for Single Site Events with respect to Multi Site Events. This is due to the fact that in *BEGes* only holes contribute to the signal and to the specific electric field profile; thus holes migrate towards the  $p^+$  electrode with very similar paths, independently from where the energy deposition occurred. As a consequence, for a localized deposition, the maximum of the current pulse and the energy are proportional. In Fig. 7, different examples of pulse traces and the derived current pulses are shown. SSE data (top left) are expected to have a nearly Gaussian distribution of  $A/E$ , with a width determined by the noise of the

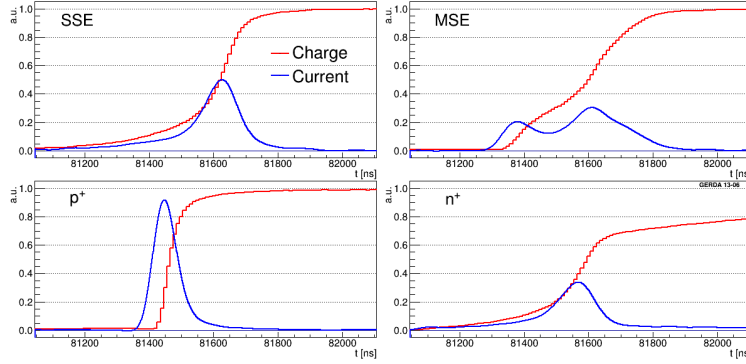


Fig. 7. Pulse traces from the BEGe detectors. The maximum of the charge pulse amplitude is set to 1 and current pulses have equal integrals. From Ref. 4, with kind permission of The European Physical Journal (EPJ).

readout electronics. The mean of the  $A/E$  values is set to one for the distribution of SSE data. In MSE events, current pulses with different drift times are clearly seen, showing that time-separated pulses are present; in this case the value of  $A/E$  is below 1. In general, for surface events near the  $p^+$  electrode,  $A/E$  is larger than 1 because both electrons and holes contribute; while for  $n^+$  surface events  $A/E$  is below unity, since only holes contribute and the current reaches its maximum at the end of the pulse. The performance of the  $A/E$  based method has been tested with calibration data. Indeed, in the  $^{228}\text{Th}$  spectrum, the double escape peak (DEP) at 1592.5 keV of the 2614.5 keV line from the  $^{208}\text{Tl}$  decay can be used as a proxy for SSE. The single escape peak (SEP) at 2103.5 keV or full energy peaks (FEP) (like e.g. at 1620.7 keV) represent MSE data. Concerning BEGes, the ratio between the maximum of the current pulse (obtained by numerical differentiation of the charge pulse)  $A$  and the energy of the event  $E$  (corresponding to the maximum of the charge pulse) is a discrimination parameter for Single Site Events with respect to Multi Site Events. This is due to the fact that in BEGes only holes contribute to the signal and to the specific field profile, which causes holes to migrate towards the  $p^+$  electrode with very similar trajectories, independently from where the energy deposition occurred. As a consequence, for a localized deposition, the maximum of the current pulse and the energy are proportional. In Fig. 7, different examples of pulse traces and the derived current pulses are shown. SSE data (top left) are expected to have a nearly Gaussian distribution of  $A/E$ , with a width determined by the noise of the readout electronics.  $A/E$  values are rescaled to match the value of unity at the mean value of the  $A/E$  distribution for SSE data. MSE events show current pulses with different drift times so that time-separated pulses are present; in this case the value of  $A/E$  is below 1. For surface events near the  $p^+$  electrode,  $A/E$  is, in general, larger than 1 because, in this case, both electrons and holes contribute, while for  $n^+$  surface events it is below unity, since only holes contribute

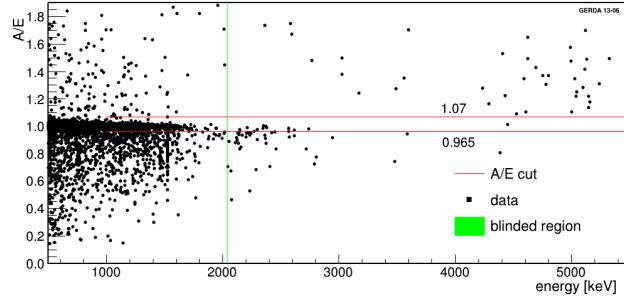


Fig. 8.  $A/E$  versus energy for the  $BEGe$  data set. The green band indicates the blinded region. The red lines indicate the acceptance region for SSE. From Ref. 4, with kind permission of The European Physical Journal (EPJ).

and the current peaks at the end of the pulse. The performance of the  $A/E$  method has been tested with calibration data. Indeed, in the  $^{228}\text{Th}$  spectrum, the double escape peak (DEP) at 1592.5 keV of the 2614.5 keV line from the  $^{208}\text{Tl}$  decay can be used as a proxy for SSE. The single escape peak (SEP) at 2103.5 keV or full energy peaks (FEP, like e.g. at 1620.7 keV) represent MSE data. No ballistic deficit is observed in the pulses of SSE events in MC simulations and also when comparing the reconstructed energy to the risetime of the pulse. The absence of such effect is also confirmed by the presence of the DEP line of  $^{208}\text{Tl}$  at the expected energy in the calibration spectrum ( $1592 \pm 0.3$  keV). A cross check of the signal detection efficiency is made using  $2\nu\beta\beta$  events, since they are genuine SSE data and homogeneously distributed in the detectors, while DEP events are not.

Fig. 8 shows  $A/E$  versus energy for the  $BEGe$  data set, together with the acceptance region obtained from data. Accepted events have  $A/E$  between 0.965 (low  $A/E$  cut) and 1.07 (high  $A/E$  cut). The lower value was determined to have less than 1% efficiency losses of the  $A/E$  Gaussian function, for energies above 1 MeV. Events below the low  $A/E$  cut are identified as MSE and  $n^+$  events, while events above the high  $A/E$  cut are discriminated as  $p^+$  electrode events. In Fig. 9 the energy spectrum of  $BEGe$  data is shown before and after the PSD cut. With a total exposure of 2.4 kg·yr for the partially unblinded  $BEGe$  data set, seven out of 40 events survive the cut in the 400 keV region around  $Q_{\beta\beta}$  (excluding the 8 keV blinded window) and the BI is reduced from  $0.042 \pm 0.007$  to  $0.007^{+0.004}_{-0.002}$  cts/(keV·kg·yr). The acceptance efficiency for signal-like events (i.e. the survival fraction of  $0\nu\beta\beta$  events) is  $0.92 \pm 0.02$  and it is derived from the survival fraction of DEP events and from Monte Carlo simulations of the  $0\nu\beta\beta$  signal. The fraction of background events, rejected at  $Q_{\beta\beta}$ , is about 80%. The method shows, therefore, a very good performance, with both high background reduction and high acceptance efficiency.

For semi-coaxial detectors, the  $A/E$  parameter does not represent a useful variable for pulse shape discrimination. Different shapes of the current pulses are, in fact, observed in the bulk volume, moving from the outer  $n^+$  surface to the  $p^+$  surface,

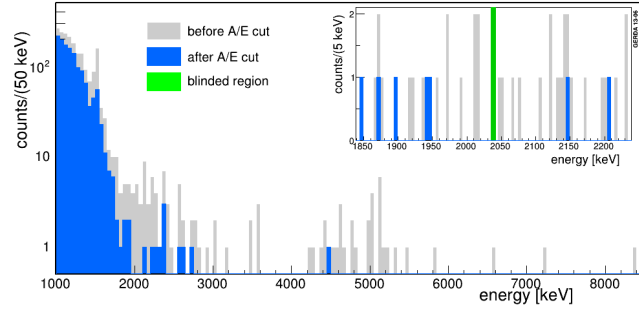


Fig. 9. Energy spectrum for the *BEGe* data set before (grey) and after (blue) the PSD cut. A zoom in the  $\pm 100$  keV window around  $Q_{\beta\beta}$  is shown in the inset. From Ref. 4, with kind permission of The European Physical Journal (EPJ).

due to the contribution of both electrons and holes to the pulse. Instead, a method based on the artificial neural network for the rising part of the charge pulses was applied. It is based on the TMlpANN<sup>37</sup> algorithm (implemented in the TMVA<sup>38</sup> toolkit of ROOT) based on multilayer perceptrons and on the so called “supervised learning” algorithm. Two hidden layers with 50 and 51 neurons were used. The times  $t_1, t_2, \dots, t_n$ , at which the 1, 3, 5, ..., 99% of the full height of the pulse is reached, were used as input parameters. Being the sampling frequency in GERDA 100 MHz, two consecutive time bins were interpolated. Calibration data were used for the network’s training; data at the DEP peak were considered as SSE and those at the full line of  $^{212}\text{Bi}$  (1621 keV) were considered as MSE. The method has been tuned to give 90% survival fraction for DEP events from the gamma line of  $^{208}\text{Tl}$  decays at 2.6 MeV. The output of the neural network is a qualifier, i.e. a number between  $\sim 0$  (background like events) and  $\sim 1$  (signal like events). Fig. 10 shows a scatter plot of this variable as a function of the energy. The qualifier threshold for 90% survival probability of DEP events was determined for each detector and each time period considered. The possible deviations from 0.90, due to an energy dependence or to a volume effect, associated to different contributions from DEP and  $0\nu\beta\beta$  events, were combined quadratically. The final value for the  $0\nu\beta\beta$  efficiency is  $0.90^{+0.05}_{-0.09}$ . The method rejects about 45% of the events in the 230 keV window around  $Q_{\beta\beta}$ . The energy spectrum before and after the PSD cut is shown in Fig. 11.

Two additional methods were used to cross check the results from neural network analysis. The first is based on a likelihood method and the second relies on the correlation between the A/E parameter and the pulse asymmetry. In the 230 keV window around  $Q_{\beta\beta}$ , about 90% of the events rejected by the neural network method were also rejected by the two other analyses.

## 6. Limit on the half-life of $0\nu\beta\beta$ decay in $^{76}\text{Ge}$

The total collected exposure of GERDA Phase I data (21.6 kg·yr) was considered to derive a limit on the half-life of  $0\nu\beta\beta$  decay in  $^{76}\text{Ge}$ <sup>5</sup>. Data were collected from

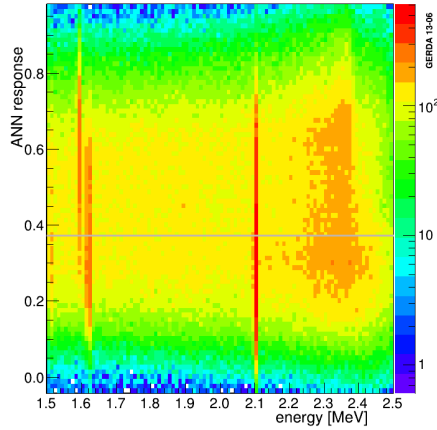


Fig. 10. Response of the TMlpANN analysis versus energy for events from  $^{228}\text{Th}$  calibrations from RG1 detector. The line at  $\sim 0.38$  corresponds to the 90% DEP survival fraction. From Ref. 4, with kind permission of The European Physical Journal (EPJ).

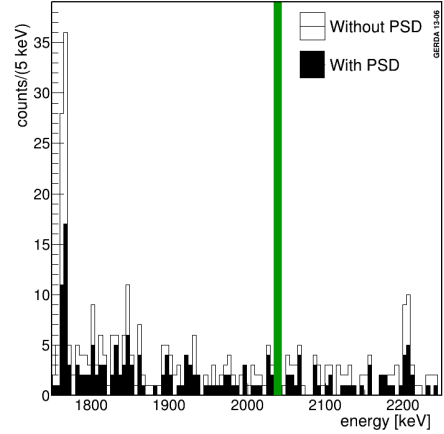


Fig. 11. Energy spectrum from semi-coaxial detectors before (open) and after (filled) the PSD selection with TMlpANN. From Ref. 4, with kind permission of The European Physical Journal (EPJ).

November 2011 to May 2013, corresponding to 492.3 live days. A fraction of 5% of the data was discarded due to temperature instabilities. Data were processed offline according to the procedure described in Ref. 39, implemented in the software tool GELATIO<sup>40</sup>. The reconstruction of the deposited energy is made by a digital filter with semi-Gaussian shaping. The energy scale of the individual detectors is determined by weekly calibrations with  $^{228}\text{Th}$  sources. The exposure-weighted average energy resolution (FWHM), extrapolated at  $Q_{\beta\beta}$ , is  $(4.8 \pm 0.2)$  keV for semi-coaxial detectors and  $(3.2 \pm 0.2)$  keV for BEGes. The energy resolution of the detectors is slightly degraded with respect to the value determined by the HdM experiment. Indeed, the detectors are placed directly in LAr and not in a standard vacuum cryostat and also there is a relatively long distance (about 30 cm) between the diode and the front-end electronics. Of course a better resolution would result in an even better sensitivity for the half-life of the  $0\nu\beta\beta$  decay. Recent studies to improve the resolution of GERDA detectors are very promising<sup>41</sup>.

A blind analysis was performed to avoid biases in the event selection criteria. The subdivision of data into subsets and the blinding procedure have already been described in Sect. 4. Different analysis cuts were applied to discard possible background signals: (i) only events with energy deposition in a single detector are accepted (anti-coincidence cut). This cut reduces background around  $Q_{\beta\beta}$  of about 15%. (ii) events from detectors in coincidence within  $8 \mu\text{s}$  with a signal from muon veto are rejected. An additional 7% reduction of the background is obtained. (iii) events preceded or followed by an other event within 1 ms are rejected. This cut rejects events from the  $^{214}\text{Bi}$ - $^{210}\text{Po}$  cascade in the  $^{222}\text{Rn}$  decay chain. The back-



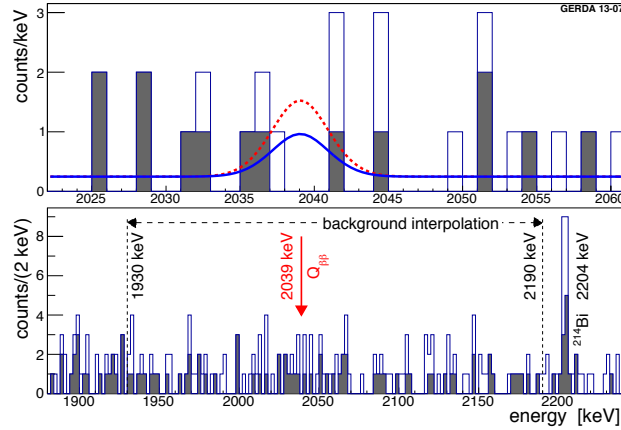


Fig. 12. Energy spectrum from all  $^{76}\text{Ge}$  detectors with (filled) and without (open) the PSD selection. In the upper panel the expectation based on the central value of the half-life predicted by Ref. 10 is also shown (red), together with the 90% C.L. limit predicted by GERDA Phase I (blue). In the lower panel the energy window used for the background interpolation is indicated. Plot from Ref. 5.

ground reduction by this cut is less than 1%.

In addition to the previous cuts, pulse shape discrimination (described in Sect. 5) was applied. The total energy spectrum, before and after the PSD selection, is shown in figure 12. The background is flat in the  $Q_{\beta\beta} \pm 5$  keV range and seven events are observed while  $5.1 \pm 0.5$  are expected from background counts. After the PSD cut, three of the six events from the semi-coaxial detectors and the one from the BEGe detector were classified as background. No event remained in the energy window  $Q_{\beta\beta} \pm \sigma_E$  and, therefore, no excess of events was present.

The half-life on the  $0\nu\beta\beta$  decay is calculated according to Eq. 5. For GERDA, the efficiency factor  $\epsilon$  contains the following terms:

$$\epsilon = f_{76} \cdot f_{av} \cdot \epsilon_{fep} \cdot \epsilon_{psd} \quad (7)$$

where  $f_{76}$  is the fraction of  $^{76}\text{Ge}$  atoms in Ge,  $f_{av}$  is the active volume fraction,  $\epsilon_{fep}$  is the probability for a  $0\nu\beta\beta$  decay to release its entire energy into the active volume and  $\epsilon_{psd}$  is the efficiency of the PSD analysis.

The analysis to derive the signal strength was performed according to a profile likelihood fit on the three GERDA data sets. The fitted function contains three constant terms for the background from the three data sets and a Gaussian peak, centered at  $Q_{\beta\beta}$  and with standard deviation equal to the energy resolution (FWHM). The four corresponding parameters of the function were the three terms for the background and  $1/T_{1/2}^{0\nu}$ , the latter being proportional to the peak counts (see Eq. 5) and common to the three subsets. The best fit value obtained is  $N^{0\nu}=0$  pointing out that no excess above background is found. The limit on the half-life is

$$T_{1/2}^{0\nu} > 2.1 \cdot 10^{25} \text{ yr (90\% C.L.)}. \quad (8)$$

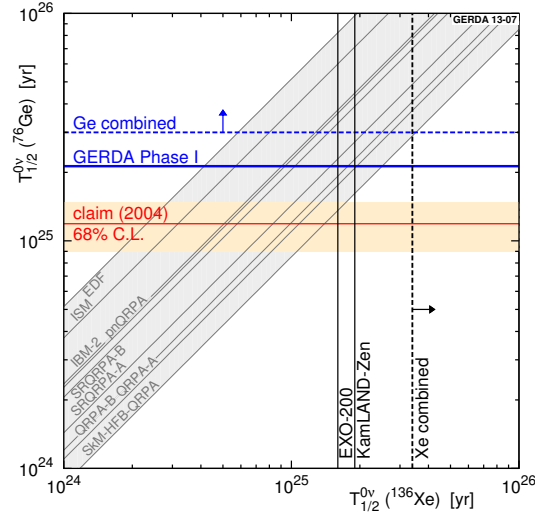


Fig. 13. 90% C.L. limits on  $T_{1/2}^{0\nu}$  for  $^{76}\text{Ge}$  and  $^{136}\text{Xe}$ , compared with the signal claim of Ref. 10. The shaded gray bands indicate the predictions for the correlation of half-lives in  $^{76}\text{Ge}$  and  $^{136}\text{Xe}$ , according to the different NME calculations considered. Plot from Ref. 5.

The systematical uncertainties due to detector parameters, selection efficiency, energy resolution and energy scale, were folded into the half-life estimation; they weaken the limit by about 1.5%. The corresponding limit on the number of signal events is  $N^{0\nu} < 3.5$  counts. The median sensitivity for the 90% C.L. limit, given the background levels and the efficiencies, is  $T_{1/2}^{0\nu} > 2.4 \cdot 10^{25}$  yr. A Bayesian analysis<sup>24</sup> was also performed (using the BAT toolkit<sup>30</sup>) with the same fit and a flat prior distribution for  $1/T_{1/2}^{0\nu}$  between 0 and  $10^{-24}$   $\text{yr}^{-1}$ . The corresponding result for the limit on the half-life is  $T_{1/2}^{0\nu} > 1.9 \cdot 10^{25}$  yr, with a median sensitivity of  $T_{1/2}^{0\nu} > 2.0 \cdot 10^{25}$  yr.

The GERDA result does not support the previous claim of  $0\nu\beta\beta$  decay observation in  $^{76}\text{Ge}$ <sup>10</sup>. Rescaling the number of counts corresponding to the half-life from Ref. 10, GERDA should observe  $(5.9 \pm 1.4)$   $0\nu\beta\beta$  decays at  $Q_{\beta\beta} \pm 2\sigma_E$  with  $(2.0 \pm 0.3)$  background events, while only 3 events were actually observed in this energy window. The Bayes factor, i.e. the ratio between the posterior probability of the model  $H_1$  (assuming the value of  $T_{1/2}^{0\nu}$  from Ref. 10) and the posterior probability of the model  $H_0$  (assuming only background), is  $P(H_1)/P(H_0) = 0.024$ .

The limit found by GERDA is consistent with the limits found from the HdM and IGEX experiments. A combined profile likelihood of the three results gives  $N^{0\nu} = 0$  as best fit and:

$$T_{1/2}^{0\nu} > 3.0 \cdot 10^{25} \text{ yr (90\% C.L.)}. \quad (9)$$

A Bayesian analysis gives the same limit and a Bayes factor of  $P(H_1)/P(H_0) = 2 \cdot 10^{-4}$ .

Results from  $^{76}\text{Ge}$  experiments can be compared to the recent limits from KamLAND-Zen<sup>42</sup> and EXO-200<sup>43</sup> on  $^{136}\text{Xe}$  half-life, assuming that the  $0\nu\beta\beta$  process is due to the exchange of a light Majorana neutrino. In this case the ratio of the  $0\nu\beta\beta$  half-lives is proportional to the square of the ratio between the nuclear matrix elements  $M_{0\nu}(^{76}\text{Ge})/M_{0\nu}(^{136}\text{Xe})$ . In Fig. 13 the limits set on  $T_{1/2}^{0\nu}$  for  $^{76}\text{Ge}$  and  $^{136}\text{Xe}$  by the different experiments are shown, together with different NME calculations and the limit found from the combination of GERDA, KamLAND-Zen and EXO-200 results. Considering the most conservative value for the NME, the Bayes Factor obtained by this combination is 0.0022. The claim is again strongly disfavoured. It is worth to note that other theoretical calculations could lead to smaller NME ratios and, consequently, to weaker conclusions.

Considering the most recent value for the  $^{76}\text{Ge}$  phase-space factor<sup>34</sup> and the NME calculations reported in Refs. from 44 to 50 (scaling the different  $g_A$  and  $R_A$  parameters according to Ref. <sup>51</sup>), the derived upper limits on the effective electron neutrino mass range between 0.2 and 0.4 eV.

## 7. Conclusions

The Gerda experiment has completed the Phase I with a total collected exposure of 21.6 kg·yr. No events from  $0\nu\beta\beta$  decay have been observed and a lower limit on the half-life on the  $0\nu\beta\beta$  decay for  $^{76}\text{Ge}$  has been estimated to be  $T_{1/2}^{0\nu} > 2.1 \cdot 10^{25}$  yr at 90% C.L. The previous claim for a  $0\nu\beta\beta$  signal<sup>10</sup> ( $T_{1/2}^{0\nu} = 1.19 \cdot 10^{25}$  yr) is strongly disfavoured by the GERDA result. The GERDA result was not compared to the value  $T_{1/2}^{0\nu} = 2.23 \cdot 10^{25}$  yr obtained from the re-analysis of HdM data because of some inconsistencies in the analysis already pointed out in Ref. 12. In the future Phase II of GERDA, the expected sensitivity on the half-life for  $0\nu\beta\beta$  decay will be about 10 times higher than Phase I,  $T_{1/2}^{0\nu} > 10^{26}$  yr; as a result, lower values of the effective Majorana neutrino mass will be explored.

## References

1. The GERDA collaboration, *Eur. Phys. J. C* **73**, 2330 (2013).
2. The GERDA collaboration, *J. Phys. G: Nucl. Part. Phys.* **40**, 035110 (2013).
3. The GERDA collaboration, *submitted to Eur. Phys. J. C*, arXiv:1306.5084.
4. The GERDA collaboration, *Eur. Phys. J. C* **73**, 2583 (2013).
5. The GERDA collaboration, *Phys. Rev. Lett.* **111**, 122503 (2013).
6. The GERDA collaboration, *Letter Of Intent*, (2004).
7. The GERDA collaboration, *Proposal*, (2004) <http://www.mpi-hd.mpg.de/GERDA>.
8. H.V. Klapdor-Kleingrothaus et al., *Eur. Phys. J. A* **12**, 147 (2001).
9. C.E. Alseth et al., *Phys. Rev. D* **65**, 092007 (2002).
10. H.V. Klapdor-Kleingrothaus et al., *Phys. Lett. B* **586**, 198 (2004).
11. H.V. Klapdor-Kleingrothaus and I.V. Krivosheina, *Mod. Phys. Lett. A* **21**, 1547 (2006).
12. B. Schwingenheuer, *Ann. Phys.* **525**, 269 (2013).
13. H.V. Klapdor-Kleingrothaus et al., *Nucl. Instr. Methods A* **481**, 149 (2002).
14. V.D. Ashitkov et al., *Instr. and Exp. Techn.* **46**, 153 (2003).

15. V. A. Rodin, A. Fässler, F. Šimkovic and P. Vogel, *Nucl. Phys. A* **766**, 107 (2006).
16. V. A. Rodin, A. Fässler, F. Šimkovic and P. Vogel, *Nucl. Phys. A* **793**, 213 (2007) (erratum).
17. F. Simkovic, R. Hodak, A. Fässler and P. Vogel, *Phys. Rev. C* **83**, 015502 (2011).
18. E. Caurier, F. Nowacki and A. Poves, *Phys. Lett. B* **711**, 62 (2012).
19. J. Barea and F. Iachello, *Phys. Rev. C* **79**, 044301 (2009).
20. J. Suhonen and O. Civitarese, *J. Phys. G: Nucl. Part. Phys.* **39**, 085105 (2012).
21. E.-W. Grewe et al., *Phys. Rev. C* **78**, 044301 (2008).
22. J. H. Ties et al., *Phys. Rev. C* **86**, 014304 (2012).
23. R. Aggarwal and A. Caldwell, *Eur. Phys. J. Plus* **127**, 24 (2012).
24. A. Caldwell and K. Kröninger, *Phys. Rev. D* **74**, 092003 (2006).
25. M. Boswell et al., *IEEE Trans. Nucl. Sci.* **58**, 1212 (2011).
26. The Geant4 collaboration, *Nucl. Instrum. Methods A* **506**, 250 (2003).
27. The Geant4 collaboration, *IEEE Trans. Nucl. Sci.* **53**, 270 (2006).
28. V. Tretyak and Yu G. Zdesenko *At. Data Nucl. Tables* **61**, 43 (1995).
29. O. A. Ponkratenko, V. I. Tretjak and Yu. G. Zdesenko, *Phys. At. Nucl.* **63**, 1282 (2000).
30. A. Caldwell, D. Kollar and K. Kröninger, *Comput. Phys. Commun.* **180**, 2197 (2009).
31. A. S. Barabash, *Phys. Rev. C* **81**, 035501 (2010).
32. C. Dörr and H. V. Klapdor-Kleingrothaus, *Nucl. Instrum. Methods A* **513**, 596 (2003).
33. A. M. Bakalyarov, A. Y. Balysh, S. T. Belyaev, V. I. Lebedev and S. V. Zhukov, *Phys. Part. Nucl. Lett.* **2**, 77 (2005).
34. J. Kotila and F. Iachello, *Phys. Rev. C* **85**, 034316 (2012).
35. G. Meierhofer et al., *Eur. Phys. J. A* **48**, 20 (2012); and references therein.
36. L. Pandola et al., *Nucl. Instr. Methods A* **570**, 149 (2007).
37. for documentation see <http://root.cern.ch/root/html/TMultiLayerPerceptron.html>
38. for documentation see <http://tmva.sourceforge.net>
39. M. Agostini et al., *J. Phys.: Conf. Ser.* **368**, 012047 (2012).
40. M. Agostini et al., *J. Instrum.* **6**, P08013 (2011).
41. G. Benato et al., *Poster at TAUP 2013 Conference*, Asilomar, (2013).
42. A. Gando et al., *Phys. Rev. Lett.* **110**, 062502 (2013).
43. M. Auger et al., *Phys. Rev. Lett.* **109**, 032505 (2012).
44. T. R. Rodriguez and G. Martinez-Pinedo, *Phys. Rev. Lett.* **105**, 252503 (2010).
45. J. Menendez et al., *Nucl. Phys. A* **818**, 139 (2009).
46. J. Barea, J. Kotila, and F. Iachello, *Phys. Rev. C* **87**, 014315 (2013).
47. J. Suhonen and O. Civitarese, *Nucl. Phys. A* **847**, 207 (2010).
48. A. Meroni, S. T. Petcov, and F. Simkovic, *JHEP* **1302**, 25 (2013).
49. F. Simkovic, V. Rodin, A. Faessler, and P. Vogel, *Phys. Rev. C* **87**, 045501 (2013).
50. M. T. Mustonen and J. Engel, *Phys. Rev. C* **87**, 064302 (2013).
51. A. Smolnikov and P. Grabmayr, *Phys. Rev. C* **81**, 028502 (2010).